Title
Lowering Ternary Oxide Synthesis Temperatures by Solid-State Cometathesis Reactions

Journal
Chemistry of Materials, 33(10)

ISSN
0897-4756

Authors
Wustrow, Allison
Huang, Guanglong
McDermott, Matthew J
et al.

Publication Date
2021-05-25

DOI
10.1021/acs.chemmater.1c00700

Lowering Ternary Oxide Synthesis Temperatures by Solid State Cometathesis Reactions

Allison Wustrow,[†] Guanglong Huang,[‡] Matthew J. McDermott,[¶,§] Daniel O'Nolan,[‖] Chia-Hao Liu,[⊥] Gia Thinh Tran,[†] Brennan C. McBride,[†] Shyam S. Dwaraknath,[¶] Karena W. Chapman,[‖] Simon J. L. Billinge,[⊥,#] Kristin A. Persson,[@,§] Katsuyo Thornton,[‡] and James R. Neilson[*,†]

†*Department of Chemistry, Colorado State University, Fort Collins, Colorado 80523-1872, USA*

‡*Department of Materials Science and Engineering, University of Michigan, Ann Arbor, Michigan 48109 USA*

¶*Materials Sciences Division, Lawrence Berkeley National Laboratory, 1 Cyclotron Road, Berkeley, California 94720, USA*

§*Department of Materials Science and Engineering, University of California, Berkeley, California 94720, USA*

‖*Department of Chemistry, Stony Brook University, Stony Brook, New York 11790-3400, USA*

⊥*Department of Applied Physics and Applied Mathematics, Columbia University, New York, New York 10027, USA*

#*Condensed Matter Physics and Materials Science Department, Brookhaven National Laboratory, Upton NY 11973, USA*

@*Molecular Foundry, Lawrence Berkeley National Laboratory, 1 Cyclotron Road, Berkeley, California 94720, USA*

E-mail: james.neilson@colostate.edu

Abstract

Low temperature synthesis routes are necessary for selectively synthesizing many metastable solid state materials. Here we identify a cooperative effect that starting materials have in lowering temperatures in solid state metathesis reactions by studying the formation of yttrium manganese oxide. Previous studies have shown that $YMnO_3$ can be synthesized by ternary metathesis with an alkali halide being produced as a secondary product. In this contribution, we show that by using alkaline earth metals instead of alkali metals, the polymorph selectivity of the reaction is changed, as orthorhombic $YMnO_3$ forms at lower temperatures than the hexagonal polymorph. Reactions were studied using *ex post facto* synchrotron X-ray diffraction. These experiments reveal that reactions using alkaline earth manganese oxides as a starting material require high temperatures to progress. Reaction temperatures can be lowered from 700 °C to 550 °C while maintaining phase selectivity by reacting both $MgMn_2O_4$ and $CaMn_2O_4$ with YOCl in a cooperative "cometathesis" reaction. The nascent halide salts appear to improve the reaction kinetics. Since the onset temperature for $YMnO_3$ formation falls 50 °C below the $MgCl_2$-$CaCl_2$ liquidus, the enhanced reactivity is consistent with surface melting of a nasscent salt biproduct at the interfaces. Cometathesis routes have similar phase selectivity and temperature reduction in reactions that form $TbMnO_3$, $ErMnO_3$, and $DyMnO_3$. Cometathesis lowers reaction temperatures while preserving reaction selectivity of the end members, making it a valuable approach for synthesizing metastable targets.

Introduction

Many solid-state reactions occur at high temperatures to overcome diffusion barriers (T >1000 °C), resulting in formation of the most stable phase at a given composition. Lowering the reaction temperature in solid-state chemistry allows for kinetic control and the possibility of synthesizing materials selectively, including metastable compounds.[1,2] Solution phase and hydrothermal synthesis routes[3] have been used to overcome the inherently low diffusion in solids at low temperature; however, solution reactions require the precursor solubility, speciation of relevant components, and

a triggered precipitation with control over both nucleation and growth process. Molten flux synthesis (e.g., a solvent that is solid at room temperature) lowers reaction temperatures by partially dissolving reagents in a molten compound which must be subsequently removed after synthesis.[4] Solid-state metathesis reactions that produce a separable and sacrificial salt byproduct often proceed at lower temperatures relative to the direct analogous reactions and can operate at rates in the limit of rapid, self-propagating reactions (e.g. 1-5 seconds)[5] or in the limit of slower, controlled reactions that require heating to several hundreds of degrees (Celsius) for multiple hours in the synthesis of oxides.[6] For example, direct formation of $YMnO_3$ from the reaction of Y_2O_3 and Mn_2O_3 requires temperatures of 1200 °C,[7] while formation from an alkali halide flux has been reported at 700-900 °C.[8] Yet, ternary metathesis reactions of the form:

$$A_x\mathrm{MnO_2} + \mathrm{YOCl} \longrightarrow A_x\mathrm{Cl} + \mathrm{YMnO_3} \tag{1}$$

where A is an alkali (x=1) or alkaline earth (x=0.5) metal, generally react in the 500-900 °C range; the metathesis reaction is faster than the binary oxides reacting with a fully molten flux.[9] As we previously showed, lowering the reaction temperature tends to impart product selectivity,[10,11] particularly with respect to $YMnO_3$ polymorph formation.

Yttrium manganese oxide ($YMnO_3$) is known to form in two polymorphs, the layered hexagonal phase[12] (h-$YMnO_3$) and the perovskite orthorhombic phase[13] (o-$YMnO_3$) (Figure 1). While many compounds of the form $Ln\mathrm{MnO_3}$, where Ln is a lanthanide, are known to exist in both polymorphs, the relative radii of Y^{3+} and Mn^{3+} allow for the two polymorphs of $YMnO_3$ to have similar formation energies,[14] making the system susceptible to "kinetic factors."[15] The traditional solid-state method of combining yttrium oxide and manganese (III) oxide and heating to very high temperature yields the thermodynamic h-$YMnO_3$,[7] while o-$YMnO_3$ has been synthesized using high pressure,[13] sol gel,[16] and flux[8] synthesis routes. The orthorhombic polymorph results from assisted metathesis reactions involving lithium carbonate and excess oxygen, which allows reactions at lower temperatures.[10] Recent computational work has shown that small amounts of

cation vacancies ($\sim$ 2%) stabilize o-$YMnO_3$ relative to the hexagonal polymorph.[11] In the same work, we reported that ternary metathesis with *A*=Li results in the formation of a mixture of the two polymorphs, owing to charge disproportionation in the lithium manganese oxide intermediates forming diverging reaction pathways. The slightly oxidized intermediate stabilizes o-$YMnO_3$ while the slightly reduced intermediate favors h-$YMnO_3$. The similar formation energies of the two polymorphs of $YMnO_3$ make it a useful target for studying reaction pathways.

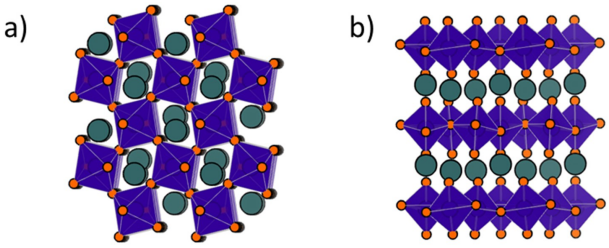

Figure 1: Structure of (a) perovskite o-$YMnO_3$ with 6 coordinate Mn and (b) h-$YMnO_3$ which is a pseudo-layered phase with 5 coordinate Mn. Despite the different structures, the two polymorphs have similar formation energies.[14]

This work reports the phase-pure synthesis of o-$YMnO_3$ using alkaline earth "cometathesis" reactions, in which two different alkaline earth-based precursors are mixed together to reduce reaction temperatures. The alkaline earth manganese oxides ($MgMn_2O_4$ or $CaMn_2O_4$) react with YOCl to selectively form the orthorhombic polymorph; however, the reactions require higher temperatures than the analogous reaction with Li ($\sim$ 600 °C). By combining both $MgMn_2O_4$ and $CaMn_2O_4$ into the same reaction vessel, the onset reaction temperature ($\sim$ 550 °C) is lowered by over 100 °C while maintaining the same product selectivity. Using a gradient furnace in combination with synchrotron X-ray diffraction (SXRD) with a focused spot to rapidly study many isothermal reactions at different temperatures *ex post facto*,[17] we show how the two alkaline earth manganese oxides influence the reaction pathway of the other, with initial formation of a Mg-Ca halide salt solution. Crystalline solid halide salts are detected at temperatures at which $YMnO_3$ forms, as the reaction temperature falls $\sim$ 50 °C below the nominal eutectic melting point of the $MgCl_2$-$CaCl_2$ phase diagram. These observations are consistent with the surface melting of the nascent halide salt at the interface to yield a high mobility reaction interface. We employ heat transfer simulations to

asses the ability of the reaction enthalpy to locally melt salt formed at the interface. We also extend this chemistry beyond the $YMnO_3$ system, demonstrating low-temperature selective synthesis of the orthorhombic polymorph for other *Ln*MnO_3 compounds, including those which typically form hexagonal polymorphs in conventional ceramic reactions (e.g., $ErMnO_3$.

Methods

Experimental procedures

*Ln*OCl (*Ln*=Tb, Dy, Y, Er) was synthesized by heating *Ln*Cl_3 hydrate in air at 400 °C for 4 h.[18] $CaMn_2O_4$ was synthesized by mixing $CaCO_3$ and MnO_2 in a 1:2 molar ratio and heating to 1300 °C for 2 weeks in air, with regrinding every 4 days.[19] $MgMn_2O_4$ was synthesized through a sol-gel route, in which $Mg(NO_3)_2$ and $Mn(NO_3)_2 \cdot 6H_2O$ were dissolved in water with a molar excess of citric acid. After stirring for 3 h, the mixture was heated to allow the water to boil off, leaving behind an orange foam. The orange foam was heated to 650 °C and cooled slowly.[20] The slow cooling is performed to prevent site mixing (i.e., site inversion) between Mg and Mn sites in the spinel structure. Orthorhombic *Ln*MnO_3 was synthesized by mixing $CaMn_2O_4$, $MgMn_2O_4$ and *Ln*OCl in a 3:1:8 molar ratio and heating at 600 °C for 48 hours. Synthesis of phase pure materials was confirmed by laboratory powder X-ray diffraction (PXRD) data collected on a Bruker D8 Discover diffractometer using Cu Kα radiation and a Lynxeye XE-T position-sensitive detector. *Ex situ* experiments were performed in an alumina crucible sealed in a fused quartz tube under vacuum, but reagents were stored and handled in air. Samples were heated at 5 °C/min to the target temperature in a muffle furnace. Diffraction patterns of *ex situ* samples were taken with a Bruker D8 Discover diffractometer, and synchrotron X-ray diffraction (SXRD) patterns were taken at the high-resolution diffractometer on the 11-BM beamline at the Advanced Photon Source.[21] Scanning electron microscopy (SEM) images were taken using a JEOL JSM-6500F field emission scanning electron microscope with a 15 kV accelerating voltage and a working distance of 10 microns. Samples were coated with 20 nm of gold to improve conductivity.

Isothermal reactions heated in a temperature gradient and analyzed *ex post facto* using synchrotron x-ray diffraction (SXRD) were studied at the 28-ID-2 beamline at the National Synchrotron Light Source II in Brookhaven National Laboratory. Precursors were loaded into a 1.1 mm OD/1.0 mm ID quartz capillary, flame sealed under argon, and placed in a gradient furnace[17] with a reproducible, uneven distribution of heating elements. This creates a temperature gradient across the length of the capillary ranging from 300 °C to 800 °C, such that the beam position defines a unique temperature. Temperature calibration was performed by loading a capillary of NaCl and noting the change in lattice parameter as a function of temperature.[22] The temperature change along the length of the capillary was non-uniform with an average change of around 20 °C/mm. Repeated measurement of a standard at various times between experimental samples throughout the experiments allow us to conclude that temperatures are accurate to within 10 °C. Samples were heated for 40 min with diffraction patterns collected every twenty minutes and then cooled to room temperature before *ex post facto* diffraction patterns were taken. Quantitative analysis was performed on *ex post facto* diffraction patterns. Data were collected with a wavelength of 0.1949 Å for single component metathesis reactions, and at 0.19319 Å for cometathesis reactions. SXRD data were collected on a Perkin Elmer plate detector at a sample-to-detector distance of 1400 mm. The experimental data were reduced in real-time using the open-source analysis software xpdAn and xpdTools, which are maintained by the xpdAcq organization on GitHub (https://github.com/xpdAcq).[23]

Density functional theory calculations

Theoretical calculations were performed to determine the oxygen vacancy formation energies of $MgMn_2O_4$ and $CaMn_2O_4$ using density functional theory (DFT) as implemented in the Vienna *Ab initio* Simulation Package (VASP).[24] We used the Generalized Gradient Approximation (GGA) with Perdew-Burke-Ernzerhof (PBE) exchange-correlation functional[25] plus Hubbard-U extension (GGA + U), with $U = 3.9$ eV for Mn.[26] The Projector Augmented Wave (PAW) method[27,28] was used to model core states via a plane wave basis with an energy cutoff of 520 eV. The $MgMn_2O_4$

(mp-27510) and $CaMn_2O_4$ (mp-18844) structures were acquired from the Materials Project (MP) database.[29] Before performing vacancy calculations, we first enumerated many possible collinear magnetic orderings for each structure using a high-throughput DFT workflow,[30] re-relaxed the structures, and selected the lowest energy magnetic ordering; this resulted in final antiferromagnetic (AFM) orderings for both structures.

Oxygen vacancy formation energies were calculated for both structures via the charged-defect supercell approach with finite-size corrections developed by Freysoldt et al.[31,32] and implemented by Broberg et al.[33] in the *atomate* workflow interface.[34] The Python Materials Genomics package (*pymatgen*)[35] was used to create and process all VASP input/output files. We used a *k*-point grid density of 50/atom and supercells containing 112 atoms ($MgMn_2O_4$: 2x2x2, $CaMn_2O_4$: 4x1x1). The defect phase diagrams are shown in Supplementary Figure S1. The oxygen vacancy formation energy for each structure was determined from the corresponding defect phase diagram by self-consistent solution of the Fermi energy, E_F. In this solution scheme, E_F is varied until net charge neutrality is reached, as determined by predicted equilibrium concentrations of both defects and majority carriers at a temperature of T=800 K.

Thermochemistry calculations

Reaction free energies, $\Delta G_{\text{rxn}}(T)$, were calculated using a mixture of computed and experimental data. DFT-based atomic structures and formation enthalpies were acquired from the Materials Project (MP) database, version 2020_09_08.[29] Gibbs free energies of formation, $\Delta G_f^0(T)$, of solid DFT compounds were estimated using the machine-learned Gibbs free energy descriptor approach implemented by Bartel, et al.[36] and applied to MP data. Thermochemical data for $MgCl_2$ and $CaCl_2$ were acquired from the experimental NIST-JANAF database.[37]

Thermal Diffusion Simulations

To facilitate the understanding of thermal transport between particles $CaMn_2O_4$ and YOCl, a three-dimensional (3D) heat transfer model was built in COMSOL Multiphysics® software[38] to follow

the temperature in the particles. The detail of the thermal model is found in the Supporting Information. The model considers a spherical $CaMn_2O_4$ particle that is embedded in a composite of YOCl particles and air. We assume that the reaction that produces heat occurs at the interface between two objects and therefore heat is uniformly distributed at the interface. We assume that the simulated geometry repeats in the entire reaction domain and therefore apply a periodic boundary condition to the outer boundaries of the composite.

Results and Discussion

Overall Reaction

Isothermal reactions of either $MgMn_2O_4$ or $CaMn_2O_4$ with 2 YOCl reveal that temperatures in excess of 700-750 °C are required for substantive reactivity. In these experiments, a capillary is placed in a furnace with a well-defined thermal gradient for a given amount of time, and SXRD scans with a focused beam are taken after the capillary had cooled to room temperature (*ex post facto*). For the reaction of $MgMn_2O_4$ with YOCl, the reaction was kept at temperature for 2 h. Weight fractions of the various phases as a function of dwell temperature are shown in Figure 2. $MgMn_2O_4$ shows limited reactivity, with less than 10 wt% of any $YMnO_3$ phase present at 750 °C; only orthorhombic $YMnO_3$ formed. The onset of reactivity coincides with the melting point of $MgCl_2$ (714 °C). No crystalline intermediates were observed in the magnesium metathesis reaction. The reaction of $CaMn_2O_4$ with YOCl was heated for 80 min. $CaMn_2O_4$ is slightly more reactive, with 30 wt% of $YMnO_3$ formed at 750 °C despite a shorter heating time relative to $MgMn_2O_4$. Unlike reactions with $MgMn_2O_4$, calcium-based metathesis results in both hexagonal and orthorhombic $YMnO_3$, although about twice as much of the orthorhombic polymorph is present relative to the hexagonal polymorph (18 vs 7 wt % at 750 °C). The ternary oxide is proceeded by Y_3O_4Cl in the reaction pathway(likely variable composition, $Y_3O_{4-\delta}Cl_{1+2\delta}$); an oxygen-rich, chlorine-poor Y-O-Cl phase that has also been observed in assisted metathesis and lithium ternary metathesis reactions to make $YMnO_3$.[11] $CaCl_2$ forms concomitantly with Y_3O_4Cl as t-YOCl is consumed.

We assume that Ca and O are removed from $CaMn_2O_4$ to balance this reaction; however, we do not observe a change in the lattice parameters or site occupancies of $CaMn_2O_4$ that would accompany significant vacancy formation. While both $CaMn_2O_4$ and $MgMn_2O_4$ form small amounts of $YMnO_3$ at 750 °C, the reaction is unable to reach completion within the time frame of heating.

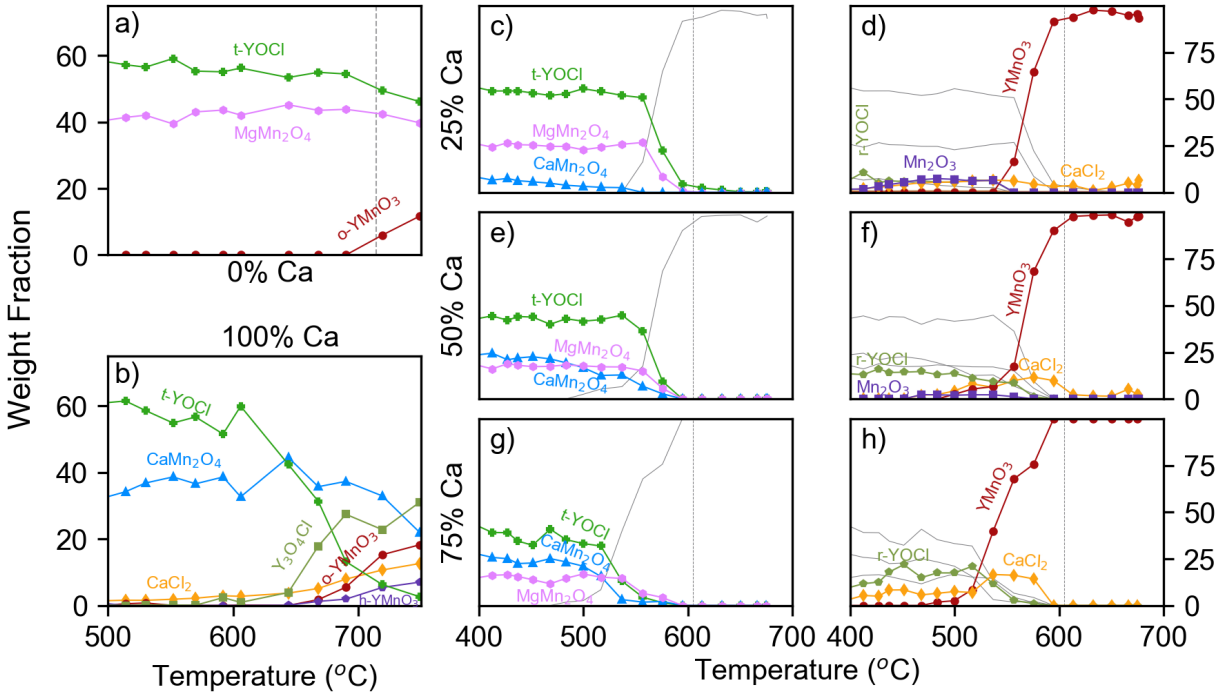

Figure 2: Phase distribution in weight fraction from isothermal reactions at different temperatures in a gradient furnace for the reaction of (a) $MgMn_2O_4 + 2YOCl$ (b) $CaMn_2O_4 + 2YOCl$ and (c-h) $xCaMn_2O_4 + (1-x)MgMn_2O_4 + 2YOCl \longrightarrow xCaCl_2 + (1-x)MgCl_2 + 2YMnO_3$ for (c,d) x =0.25, (e,f) x =0.5, and (g,h) x =0.75. Data were obtained from quantitative phase analysis of SXRD data. Phases include t-YOCl (green plus), $MgMn_2O_4$ (pink hexagon), $YMnO_3$ (red circle), $CaMn_2O_4$ (blue triangle), Y_3O_4Cl (olive square), $CaCl_2$ (yellow diamond) and h-$YMnO_3$ (purple pentagon). For cometathesis reactions, the $YMnO_3$ phase contributions were summed to a single line (red circle) The melting point of the produced halide salt in each reaction is denoted with a dashed line. The melting point of pure $CaCl_2$ is beyond the limits of this plot (772 °C). Small amounts of $CaMnO_3$ (>4 wt%) present in the starting material have been omitted for clarity.

By combining $MgMn_2O_4$ and $CaMn_2O_4$ into a single reaction mixture for a cometathesis reaction with YOCl, the $YMnO_3$ formation onset temperature is reduced from 690 °C to 550 °C. The

idealized overall balanced reaction equations take the form,

$$x\mathrm{CaMn_2O_4} + (1-x)\mathrm{MgMn_2O_4} + 2\mathrm{YOCl} \longrightarrow x\mathrm{CaCl_2} + (1-x)\mathrm{MgCl_2} + 2\mathrm{YMnO_3} \qquad (2)$$

with x denoting the relative amount of $CaMn_2O_4$ and $MgMn_2O_4$ added to the reaction. In reality, some solid solutions form upon reaction, which are discussed below. Metathesis reactions with two or more possible halide salts formed in the product are denoted as cometathesis reactions. Isothermal reactions in a temperature gradient furnace studied by SXRD were carried out at $x =$ 0.25, 0.5, and 0.75 to observe the effects of spectator cation composition on the reaction. All cometathesis reactions were heated at temperature for 40 min. Weight percents of each phase in the reaction mixture are determined from quantitative analysis of diffraction data. Weight percents of relevant phases plotted against dwell temperature is shown in Figure 2. $CaMnO_3$ is present in small amounts in Ca rich systems and is an impurity in the synthesis of $CaMn_2O_4$. The phase never comprises more than 4 wt% of the sample and reacts concurrently with $CaMn_2O_4$, and thus it is omitted from the figure for clarity. In all systems with a mixed Mg–Ca composition, the formation temperature of $YMnO_3$ is significantly decreased, with $YMnO_3$ showing up at temperatures as low as $T \sim$550 °C ($x = 0.75$). Compared to singe cation metathesis reactions, he formation temperature of $YMnO_3$ is significantly lower, and the reaction rate is significantly faster in cometathesis reactions. In single alkaline earth metathesis, $YMnO_3$ forms gradually with only 10 wt% and 20 wt% of $YMnO_3$ present in powder patterns taken after over an hour of dwelling at 800 °C in the $MgMn_2O_4$ and $CaMn_2O_4$ reactions, respectively. In contrast, in the mixed Mg-Ca cometathesis reactions, the reaction nearly progresses to completion after only 40 min of heating. $YMnO_3$ accounts for $>$ 80 wt% of crystalline phases at 600 °C, with the balance comprised of $CaCl_2$ related phases and small amounts of unreacted starting material.

In cometathesis reactions, the reactions proceed $\sim$ 50 °C below the eutectic melting point of $MgCl_2$-$CaCl_2$ mixtures (T_{eutectic} = 610 °C,[39] Figure 3). At Mg rich compositions (x=0.5, x=0.25), all $CaCl_2$ present in the sample melts once T_{eutectic} is reached. However, crystalline $CaCl_2$ is

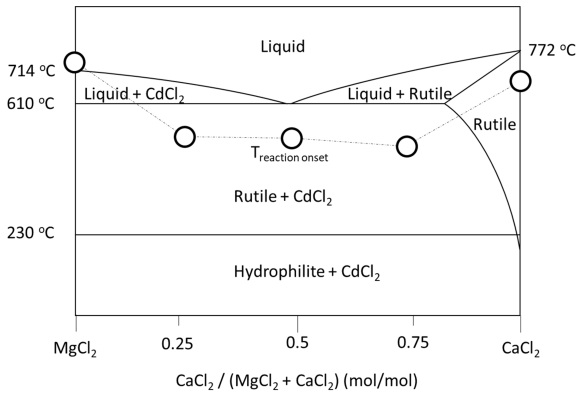

Figure 3: Phase diagram of $MgCl_2$ and $CaCl_2$, with the onset temperature of $YMnO_3$ formation at each composition marked with an open black circle. Data for the phase diagram is found in Ref. 39.

observed at temperatures where $YMnO_3$ has begun to form in *in situ* measurements. In solid state chemistry, molten fluxes are known to improve transport in systems, and are commonly used to grow single crystals;[40] however, the simultaneous presence of $CaCl_2$ and $YMnO_3$ in the same *in situ* diffraction patterns indicates that a salt does not have to be fully molten to provide a flux-like kinetic benefit.

The morphology of $YMnO_3$ produced below the salt melting point is inconsistent with bulk salt metathesis. Reactions for $x = 0.75$ were heated at 575 °C and 800 °C for 48 h *ex situ*. PXRD confirms that both samples converted completely to $YMnO_3$. Scanning electron micrographs of $YMnO_3$ reacted at 575 °C show small clumps without defined facets (Figure 4(a)). However, while some clumps were present in the 800 °C sample (Figure 4b), large hollow rods up to 50 μm in length were also formed. Elemental analysis of the rods confirmed the $YMnO_3$ composition but with a small amount of Mg also present. We attribute the hollow morphology of the $YMnO_3$ to the molten salt etching the rod face after formation; however, the exact mechanism of formation is still unclear. Regardless, the larger crystallites of $YMnO_3$ found in samples heated above the salt melting point (610 °C) is consistent with flux grown crystals, and a lack of these large crystals in the low temperature samples suggests that the salt is not completely molten during synthesis, yet complete conversion to $YMnO_3$ still occurs.

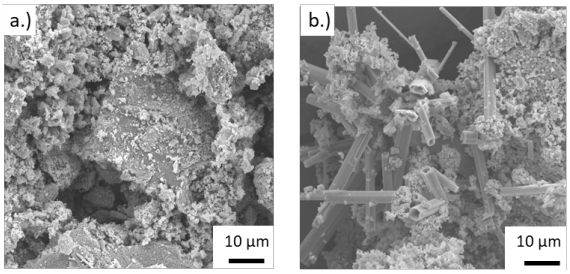

Figure 4: Scanning electron micrographs of the products from cometathesis reactions (x =0.75) performed at (a) T = 575 °C and (b) T = 800 °C. Samples were rinsed with water and then dried prior to measurement to remove hydroscopic halide salts. $YMnO_3$ formed below $T_{eutectic}$ do not show a faceted morphology, while $YMnO_3$ formed above $T_{eutectic}$ appears as faceted microrods.

As the reaction temperature approaches the halide melting temperature, the amount of $YMnO_3$ formation in the *ex post facto* cometathesis samples increases, showing a gradual rather than a sharp rise in conversion after 40 minutes of heating to increasing temperatures. While significant reactivity is seen below 600 °C in the isothermal SXRD experiments, full conversion of the starting materials to $YMnO_3$ after 40 min of heating is not observed until within 10 °C of the salt melting point. We offer three hypotheses explaining this phenomenon: 1) solids near their melting point exhibit sufficient mobility increases which allow for increased reaction rate below the bulk melting point, 2) local heating caused by reaction progress allows for melting at the oxide halide interface, increasing diffusion and therefore reaction rate, and 3) the thermometry of the gradient furnace was poorly calibrated. Hypothesis 3 is disproved by comparing the observed lattice parameters and melting point of $CaCl_2$ to both literature and *in situ* diffraction measurements of a mixture of $CaCl_2$ and $MgCl_2$ run independently. A brief discussion of the other two hypotheses follows.

As crystals approach their melting point, atomic vibrations within the structure increase in magnitude. The Lindemann criterion states that a crystal melts when the magnitude of atomic vibrations reach around 10% of the interatomic distance within the structure.[41] However, temperature is an averaged bulk property, and while the average fluctuation magnitude across a sample may not achieve the Lindemann criterion, individual atoms can have enough kinetic energy to create a liquid-like state at the surface of the structure. This phenomenon, referred to as surface melting, occurs at temperatures just below the melting point of materials such as Pb,[42] $SrTiO_3$,[43]

and DNA.[44] We posit that when the $MgCl_2$-$CaCl_2$ mixture approaches its melting point, it undergoes melting-like behavior at the surface, thus providing a relatively mobile interface to facilitate $YMnO_3$ crystallization. At higher temperatures, the liquid-like layer increases in thickness, and therefore is able to transport greater amounts of reactive species, increasing the reaction rate. $YMnO_3$ formation begins below 600 °C; however, at temperatures beneath the bulk melting point, complete conversion to $YMnO_3$ is not achieved in 40 minutes of heating. Because the molten phase appears directly at the interface between precursors, it increases the reaction rate at the interface in contrast to the similar reaction of binary oxides in a halide flux.

We also consider the possibility that local heating by the reaction could locally melt the interface in a quasi-adiabatic process, in which the heat produced by the enthalpy of reaction locally heats the salt above its melting point. Maximum reaction rates were estimated by quantifying reaction progress of *in situ* measurements taken of samples heated in the gradient furnace as a function of time. We used the thermal diffusion model and simulated the heat transfer between and within the particles. We recorded the time needed for a point at the interface between a $CaMn_2O_4$ particle and the composite consisting of the YOCl particles and air to reach the halide melting temperature (610 °C) at reaction rates observed in the experiment. The relationship between the time to reach the melting temperature (in min) and the conversion rate (in %/min) is plotted in Figure S4. At 550 °C, the onset temperature for $YMnO_3$ formation, the conversion rate was estimated from the experiment to be around 0.6 % conversion/min; at this rate, it is predicted to take roughly 99 minutes for local heating from the reaction to melt the halide salt (see Figure S4). Therefore, we conclude that the self-heating is too slow to be the cause of increased reactivity. However as the temperature approached the melting point and the reaction rate increased to approximately 13% conversion/min, it was found that the reaction could output enough heat to melt the surrounding salt in less than 5 minutes, which, in conjunction with surface melting, would produce a non-negligible effect on reaction rate in the system. While surface melting is likely the main factor contributing to the reaction rate in this case, local melting by the heat of the reaction could also become important in systems which are particularly sensitive to small temperature changes.

Both of these hypotheses rely on the presence of both $CaCl_2$ and $MgCl_2$, neither of which are initially present in the reaction. However, at temperatures around $T_{eutectic}$, the formation of the halides is autocatalytic, with the salt increasing the kinetics of forming more salt. Therefore, a small amount of nascent $CaCl_2$ and $MgCl_2$ quickly becomes noticeable on a measurable scale as temperatures are sufficiently high to enable surface melting, enabling reactivity despite not initially being present in the reaction. Tamman's rule states that the reactivity temperature in a solid state reaction is dictated by the melting point of the reactants; however, we show that the melting point of the products also play a strong role in determining the temperature of reaction.

$MgMn_2O_4$ and $CaMn_2O_4$ Reactivity

$YMnO_3$ formation is observed only after $MgMn_2O_4$ begins to react, indicating that the combined reactions of $CaMn_2O_4$ and $MgMn_2O_4$ are required to form $YMnO_3$ at low temperatures. For all three cometathesis reactions, the calcium-based post-spinel reacts at lower temperatures than the magnesium-based spinel. When the system is sufficiently calcium deficient (x = 0.25), $CaMn_2O_4$ reacts completely before $MgMn_2O_4$ starts to react, and both Ca and O are removed from the structure to form $CaCl_2$ and yttrium oxychloride intermediates, leaving crystalline bixybite Mn_2O_3 behind. Complete conversion of $CaMn_2O_4$ to Mn_2O_3 at x= 0.25 corresponds to Mn_2O_3 comprising 8 wt% of the total sample, close to the 7.5 wt% observed. While $CaMn_2O_4$ begins reacting as early as 400 °C, $MgMn_2O_4$ remains inert until 500 °C. $YMnO_3$ starts to form in significant quantity only when $MgMn_2O_4$ also begins to react. While both $MgMn_2O_4$ and $CaMn_2O_4$ are consumed to form the $YMnO_3$ final product in the cometathesis reactions, they do not react simultaneously.

As the formation of $YMnO_3$ corresponds so closely with the reaction of $MgMn_2O_4$, contraction of the $CaCl_2$ unit cell is also correlated to formation of $YMnO_3$. At temperatures greater than 605 °C, as much as 18% of the Ca^{2+} in the rutile $CaCl_2$ structure can be replaced with Mg^{2+}, resulting in a smaller unit cell.[45] $MgCl_2$ crystallizes in the rhombohedral, layered $CdCl_2$ structure. The phase is absent in *ex post facto* SXRD data; however, this could be attributed to the reactivity of Mg-based phases with the quartz capillary or Mg substituting into other phases in the pattern. In

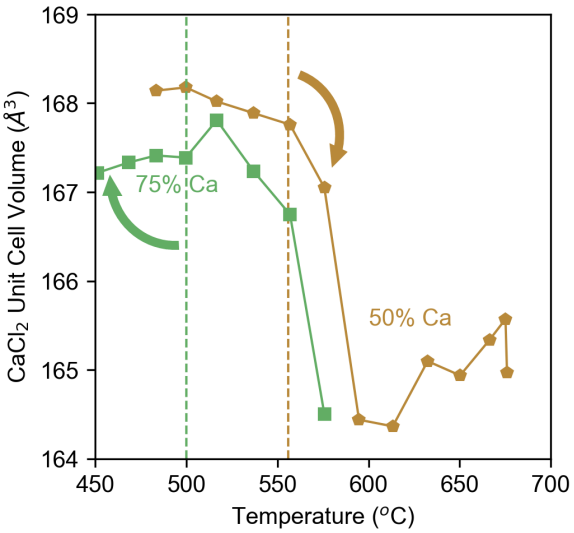

Figure 5: Unit cell volume of rutile $CaCl_2$ measured at room temperature for reactions with different dwell temperatures from *ex post facto* SXRD for samples containing 75% Ca (blue circle) and 50% Ca (green square). Onset of $MgMn_2O_4$ reactivity is indicated with a vertical dashed line in the corresponding color. The volume of $CaCl_2$ rapidly begins to drop at the reaction onset temperature, indicating that Mg^{2+} substitution has occurred.

contrast, $CaCl_2$ crystallizes in the hydrophilite structure at temperatures lower than 240 °C and in the rutile structure at higher temperatures, both of which are observed in the appropriate *in situ* diffraction patterns. The addition of magnesium to this rutile structure is easily observed. The unit cell volume of rutile-$CaCl_2$ as a function of temperature is plotted in Figure 5. The unit cell volume drops rapidly at temperatures where $MgMn_2O_4$ reacts and Mg substitutes into $CaCl_2$, suggesting that no significant amount of Mg^{2+} is released from the spinel structure before $MgMn_2O_4$ reaction is observed in the powder pattern. The contraction of the unit cell of $CaCl_2$ also corresponds with a lowering of the melting point in the halide salt (Figure 3), which in turn increases the reaction rate of $MgMn_2O_4$ and formation rate of $YMnO_3$.

The lower reaction temperature of $CaMn_2O_4$ reactivity relative to that of $MgMn_2O_4$ correlates with a more favorable reaction energy, largely a result of the greater enthalpy of formation of $CaCl_2$ (-2.793 eV/atom) relative to $MgCl_2$ (-2.254 eV/atom).[29] The alkaline earth manganese oxides have similar formation enthalpies (-2.354 eV/atom for $MgMn_2O_4$ and -2.461 eV/atom for $CaMn_2O_4$). The overall reaction of an alkaline earth manganese oxide with YOCl to form $YMnO_3$

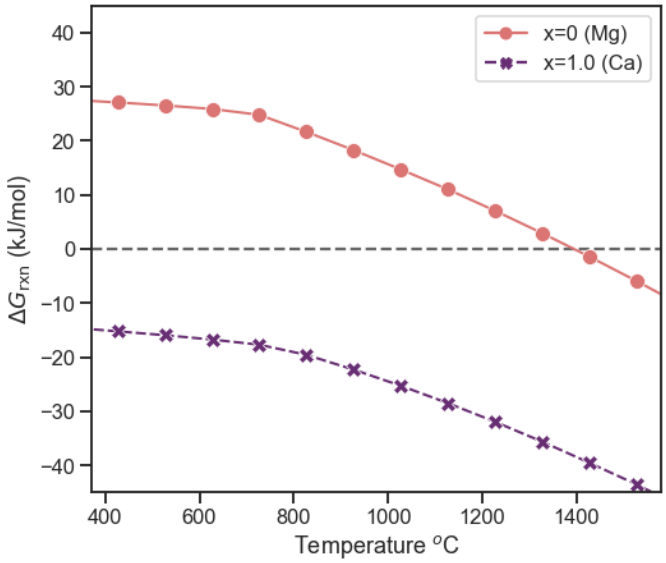

Figure 6: $\Delta G_{\text{rxn}}(T)$ of $A\text{Mn}_2\text{O}_4 + 2\text{YOCl} \longrightarrow A\text{Cl}_2 + + 2\text{YMnO}_3$, where A is Mg (orange circles) and Ca (purple x's). The change in slope corresponds to the onset of melting of MgCl_2 and CaCl_2, as reported in the experimental thermochemistry data.[37] Reactions of CaMn_2O_4 have more negative ΔG_{rxn} at all investigated temperatures.

and the corresponding halide salt is more energetically favorable in the case of CaMn_2O_4 when compared to MgMn_2O_4, with the latter reaction being energetically unfavorable at temperatures less than 1400 °C (Figure 6).[36] Experimentally, YMnO_3 is first seen forming from the reaction of pure MgMn_2O_4 and YOCl in samples which dwelled at 720 °C; however, the structure has a smaller unit cell than YMnO_3 formed in the calcium reaction, suggesting that the final product still contains Mg, which is not accounted for in the calculations shown in Figure 6. Instead of forming MgCl_2, Mg^{2+} can also react with the quartz capillary the reaction was performed in, promoting the formation of YMnO_3. The reaction with CaMn_2O_4 with YOCl is more thermodynamically favorable than that of MgMn_2O_4 and YOCl and does not rely on various side reactions to occur, allowing for the formation of YMnO_3 at lower temperatures.

The availability of defect-mediated reaction pathways plays a role in the lower temperature reactivity of CaMn_2O_4. The tolerance of CaMn_2O_4 to oxygen vacancies enables a robust intermediate chemistry at low temperatures, which is inaccessible to the vacancy-resistant MgMn_2O_4 structure. A balanced reaction corresponding to the observed intermediates in reactions of CaMn_2O_4

and YOCl is shown in Equation 3, with ε representing the extent of reaction bounded by $0 \leq \varepsilon \lesssim 0.33$,

$$CaMn_2O_4 + 2\,YOCl \longrightarrow 2\,\varepsilon CaCl_2 + Ca_{1-2\varepsilon}Mn_2O_{4-2\varepsilon} + 2\,YO_{1+\varepsilon}Cl_{1-2\varepsilon} \longrightarrow CaCl_2 + 2\,YMnO_3 \tag{3}$$

In other words, the initial reaction pathway for $CaMn_2O_4$ involves the loss of both Ca^{2+} and O^{2-} from the structure. As oxidative deintercalation of cations is known in both spinel and post spinel structures, we focused on comparing the energetic penalty required to remove an oxygen reductively from both $MgMn_2O_4$ and $CaMn_2O_4$. Using DFT and the point defect calculation method implemented by Broberg, et al.,[33] we find that 1.55 eV/vacancy is required to create an oxygen vacancy in $MgMn_2O_4$, compared to 1.23 eV/vacancy in $CaMn_2O_4$. The relative difference between the two values is small, but significant. This difference in energetics is manifested in the Y-O-Cl intermediates that form along the reaction pathway. The structure of the yttrium oxide chloride phase changes with increasing reaction progress, ε, changing from a layered tetragonal structure (t-YOCl) to a rhombohedral one (r-YOCl) before transitioning into a channeled structure (Y_3O_4Cl), as Ca from $CaMn_2O_4$ reacts with removed Cl to form $CaCl_2$ and oxygen is abstracted from $CaMn_2O_4$. For simplicity's sake, the Y-O-Cl containing phases are referred to by their idealized stoichiometry, but charge balance dictates that all three structures take the form of $YO_{1+\varepsilon}Cl_{1-2\varepsilon}$ with increasing values of epsilon. The oxygentation of Y-O-Cl intermediates as the reaction progresses has been observed in similar reactions.[9,11] By varying x (relative amounts of $MgMn_2O_4$ and $CaMn_2O_4$) and changing the $CaMn_2O_4$ to YOCl starting ratio, the extent to which YOCl reacts before $YMnO_3$ forms can be tuned. At low concentrations of $CaMn_2O_4$, Mn_2O_3 is produced stoichiometrically as an intermediate as ε approaches the total amount of Ca at lower temperatures, as observed for x = 0.25 and 0.5 (Figure 2). For x = 0.25, compete conversion of $CaMn_2O_4$ to Mn_2O_3 is observed. Higher amounts of r-YOCl are observed with increased amounts of $CaMn_2O_4$ (e.g., x = 0.75), extending to observation of only the oxygen rich and chlorine poor Y_3O_4Cl phase in the x = 1 reaction. $MgMn_2O_4$ does not appear to participate in the formation of

Y-O-Cl intermediates, and $MgMn_2O_4$ must react directly to form $YMnO_3$, limiting its accessible chemistry at low temperatures.

$YMnO_3$ Polymorph Distribution

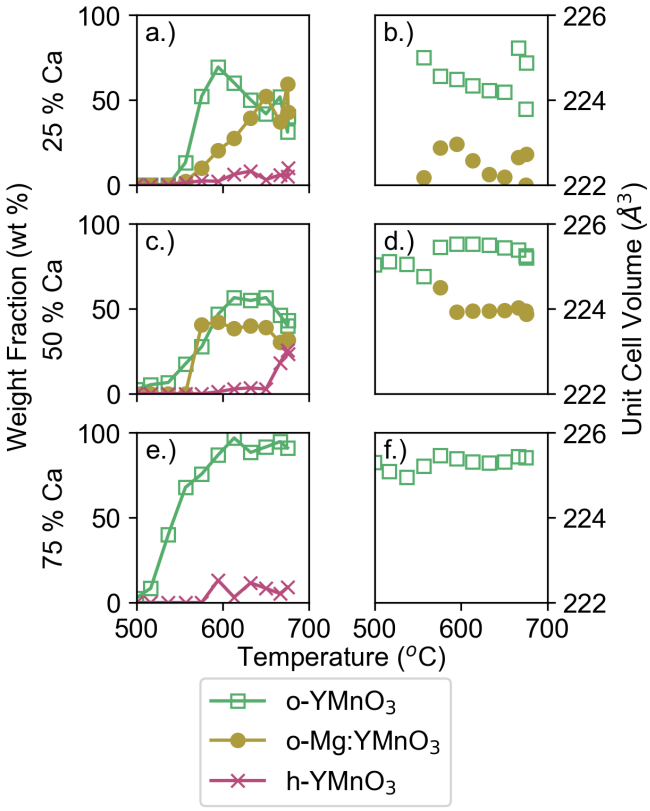

Figure 7: Polymorph distribution of $YMnO_3$ as a function of temperature for $x = 0.25$ (top), $x = 0.5$ (center), and $x = 0.75$(bottom). o-$YMnO_3$ is denoted by green squares, o-Mg:$YMnO_3$ is denoted by yellow circles, and h-$YMnO_3$ is denoted by magenta hexagons. Unit cell volume (Å^3) as a function of temperature for the orthorhombic polymorphs is shown on the right. o-Mg:$YMnO_3$ is formed in samples with high Mg concentrations and is distinguished from unsubstituted o-$YMnO_3$ by its smaller unit cell.

In all cometathesis reactions studied here, perovskite type o-$YMnO_3$ forms before the layered h-$YMnO_3$ (Figure 7). The compositions of $x = 0.25$ and $x = 0.75$ do not produce significant amounts of h-$YMnO_3$ after 40 min of heating; however, at the highest temperatures measured for $x = 0.5$, the hexagonal polymorph begins to form. Aliovalent substitution of Mg or Ca in the

ternary oxide as it is forming stabilizes the orthorhombic phase over the conventionally more stable hexagonal phase which can be made directly from binary oxides at 1200 °C.[7] o-$YMnO_3$ is known to be stabilized by small amounts of Mn oxidation,[11] consistent with the substitution of Y^{3+} by divalent alkaline earth metals in the structure. In fact, the solid solution of $YMnO_3$ with $CaMnO_3$ is known to transition from the hexagonal to the orthorhombic structure at 22% Ca doping.[46] Magnesium has been shown to substitute into lanthanide manganese oxides such as $YbMnO_3$,[47] and it likely could also substitute into $YMnO_3$, stabilizing the orthorhombic polymorph. However, we cannot rule out the hypothesis that o-$YMnO_3$ is more stable at lower temperatures, even in the absence of defects.[9] *Ex situ* reactions heated to 800 °C for 48 h show formation of h-$YMnO_3$ at x = 0.25, 0.5, and 0.75, demonstrating that at high temperatures and long times, the hexagonal phase is favored over the orthorhombic phase. Reactions with a higher concentration of $CaMn_2O_4$ in the starting mixture show a higher phase fraction of h-$YMnO_3$, showing a lower extent of alkaline earth metal substituting in the final product when less Mg was present in the system. The more favorable thermodynamics involved in the formation of $CaCl_2$ relative to the formation of $MgCl_2$ provides a more favorable driving force for Ca^{2+} to leave the oxide than Mg^{2+}, which results in Mg substitution in the final o-$YMnO_3$ product when large amounts of $MgMn_2O_4$ are used in the precursor mixture ($x < 0.75$).

Two closely related *Pnma* phases are present in high temperature *ex post facto* diffraction patterns, corresponding to o-$YMnO_3$ and Mg substituted o-Mg:$YMnO_3$. The Mg substituted phase is distinguished from the unsubstituted phase by a contraction of the *a* lattice parameter from 5.78 Å to 5.69 Å , similar to the structural contraction seen in oxygen rich o-$YMnO_{3+\delta}$ by Todd et al.[10] Unit cell volumes as a function of dwell temperature are seen in Figure 7. This contraction is difficult to observe in low angle peaks; however, at high angle peaks (Q>3.5 $Å^{-1}$) the two phases are readily observed (Figure S5). Under all three cometathesis conditions, o-$YMnO_3$ forms before o-Mg:$YMnO_3$, consistent with $CaMn_2O_4$ reacting before $MgMn_2O_4$. Rietveld analysis of SXRD data collected from *ex situ* reactions run at 600 °C for 48 hours with x=0.25 and x=0.75 showed a contracted o-Mg:$YMnO_3$ with 35% of the Mn site and 15% of the Y site substituted by Mg.

The other o-$YMnO_3$ phase present in each pattern showed no evidence of substitution when all site occupancies were allowed to freely refine. o-Mg:$YMnO_3$ comprises a higher phase fraction of the sample in reactions with a high Mg^{2+} concentration. Yet, no o-Mg:$YMnO_3$ is observed for x = 0.75 in the isothermal reaction SXRD data collected *ex post facto*; including the substituted phase in refinements did not improve the statistics, suggesting the absence of the phase in the measured material. At this composition (x=0.75), most of the Mg substitutes into $CaCl_2$ as it leaves the lattice. Elemental analysis by energy dispersive X-ray spectroscopy (EDS) at low x showed that after washing with water to remove halide salts, Mg remained in the sample while Ca did not, further supporting Mg doping in o-Mg:$YMnO_3$. In compositions where there is too much Mg for it all to substitute into $CaCl_2$, there is less thermodynamic driving force for Mg to leave the $YMnO_3$ structure, leading to Mg substitution. By choosing compositions with high initial $CaMn_2O_4$ concentrations, the Mg^{2+} produced in the reaction dissolves into $CaCl_2$ instead of doping o-$YMnO_3$. The mixed halide salt has a low enough melting point to promote reactivity at temperatures sufficiently low to prevent o-$YMnO_3$ from converting to h-$YMnO_3$. The reaction temperature difference obtained from cometathesis allows for the formation of a metastable oxide.

Cometathesis Reactions of *Ln*OCl

Alkaline earth cometathesis enables the low temperature phase selective synthesis of other orthorhombic *Ln*MnO_3 phases. Reactions of $CaMn_2O_4$ and $MgMn_2O_4$ were performed with *Ln*OCl (*Ln* = Tb, Dy, Er). For lanthanides with ionic radii larger than 1.02 Å (such as Tb and Dy), direct reaction of the oxides yields the orthorhombic *Ln*MnO_3 polymorph.[14] Like $YMnO_3$, direct reaction of Er_2O_3 and Mn_2O_3 results in hexagonal $ErMnO_3$, yet o-$ErMnO_3$ has been made through thin film,[48] sol gel[49] and high pressure[50] approaches, similar to $YMnO_3$. A 75/25 mol % mixture of $CaMn_2O_4$ and $MgMn_2O_4$ was mixed with a stoichiometric amount of *Ln*OCl and reacted at 600 °C for 48 h. The high calcium to magnesium ratio was chosen to inhibit Mg doping of the final lanthanide product. The low reaction temperature prevents conversion of of o-*Ln*MnO_3 to the hexagonal polymorph. Diffraction patterns of the resulting powders are shown in Figure 8. By

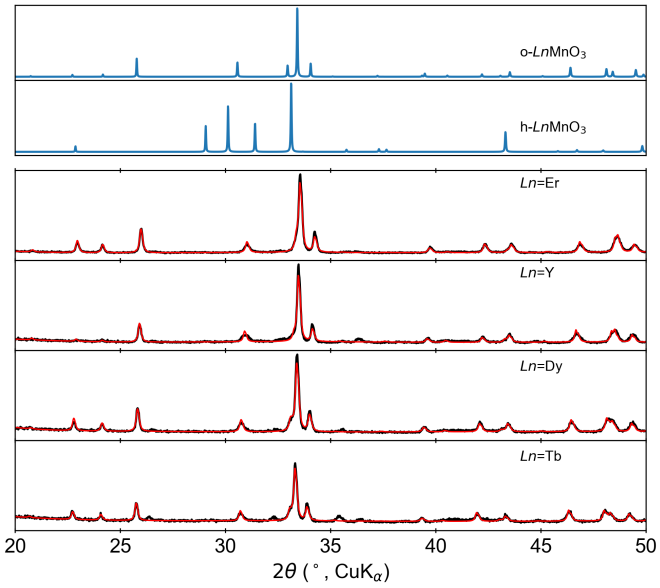

Figure 8: X-ray diffraction patterns for reactions of *Ln*OCl with $MgMn_2O_4$ and $CaMn_2O_4$ at 600°C for 48 h. Representative powder patterns for both polymorphs of *Ln*MnO_3 are shown at the top for comparison.Under these conditions, all tested lanthanides formed o-*Ln*MnO_3. Data are shown in black, and refined fits for the orthorhombic polymorph of each phase are shown in red.

observing the high-angle peaks, we determine that there is only one unsubstituted perovskite phase present in these samples, and the unit cell volumes of the phases are consistent with *Ln*MnO_3. In each case, complete conversion to orthorhombic *Ln*MnO_3 was achieved, even with the smaller Er ion. Mixtures of Ln_2O_3 and Mn_2O_3 at the same heating profile did not lead to a reaction. The lowered reaction temperature and polymorph selectivity in the alkaline earth cometathesis approach is maintained over a wide range of lanthanide manganese oxide systems.

Conclusions

Cometathesis lowers reaction temperatures in ternary metathesis reactions. By reacting a mixture of $CaMn_2O_4$ and $MgMn_2O_4$ together with YOCl, the formation temperature of $YMnO_3$ is reduced from 690 °C to 575 °C. In addition, cometathesis reactions occur rapidly when compared to their single metathesis counterparts, with >90% reaction conversion observed within 50 °C of reaction onset. We propose that surface melting of small amounts of $CaCl_2$ and $MgCl_2$ forming at the in-

terfaces enables this low temperature reactivity in an autocatalytic manner. Using alkaline earth cations in the metathesis reactions imparts a selectivity of the orthorhombic perovskite $YMnO_3$ over the hexagonal polymorph, which we attribute to Ca and Mg substitution in the $YMnO_3$ in the early stages of the reaction, stabilizing the orthorhombic phase. However, we cannot rule out the hypothesis that o-$YMnO_3$ is thermodynamically stable at lower temperatures. As the reaction progresses, Ca is removed from the $YMnO_3$ structure, however some Mg remains. Combining $CaMn_2O_4$ and $MgMn_2O_4$ does not remove the selectivity of these reactions for the orthorhombic polymorph. By studying trends in reactivity and the reaction pathway for the $YMnO_3$ system, we used the reaction design rules in chemically similar systems, as shown by the low temperature polymorph selective syntheses of $TbMnO_3$, $DyMnO_3$, and $ErMnO_3$. All three materials are synthesized in the orthorhombic polymorph without Mg doping. In cases where a metathesis reaction pathway favors a nominally metastable polymorph, cometathesis can maintain the selective pathway while lowering the overall reaction temperature, hindering conversion to a phase that may be more globally stable. By studying reaction trends and pathways, we unlock the tools for designing selective synthetic routes to materials which traditionally require high temperatures and pressures to synthesize.

Supporting Information

The following information is made available in the supporting information available on the publishers website: Defect phase diagrams for $MgMn_2O_4$ and $CaMn_2O_4$, details of the thermal diffusion modeling, and representitve diffraction patterns highlighting the difference between o-$YMnO_3$ and Mg substituted o-$YMnO_3$.

Acknowledgement

This work was supported as part of GENESIS: A Next Generation Synthesis Center, an Energy Frontier Research Center funded by the U.S. Department of Energy, Office of Science, Basic En-

ergy Sciences under Award Number DE-SC0019212. This research used resources at beamline 28-ID-2 of the National Synchrotron Light Source II, a U.S. Department of Energy (DOE) Office of Science User Facility operated for the DOE Office of Science by Brookhaven National Laboratory under Contract No. DE-SC0012704. Use of the Advanced Photon Source at Argonne National Laboratory was supported by the U. S. Department of Energy, Office of Science, Office of Basic Energy Sciences, under Contract No. DE-AC02-06CH11357. We thank Christopher L. Rom for XRD plotting software (github.com/CLRom)

Author Contributions

AW synthesized and characterized precursors. AW, GTT and BCM performed SXRD experiments. DO and KC assisted with using the gradient furnace, and CHL wrote scripts to assist with SXRD collection under the supervision of SB. AW analyzed SXRD data. MJM, SSD, and KAP performed calculations relating to reaction thermodynamics. GH and KT performed simulations of thermal diffusion within the sample. AW and JRN conceived of the study and wrote the manuscript with contributions from all authors.

References

(1) Martinolich, A. J.; Neilson, J. R. Toward reaction-by-design: achieving kinetic control of solid state chemistry with metathesis. *Chem. Mater.* **2017**, *29*, 479–489.

(2) Stein, A.; Keller, S. W.; Mallouk, T. E. Turning down the heat: design and mechanism in solid-state synthesis. *Science* **1993**, *259*, 1558–1564.

(3) Feng, S.; Xu, R. New materials in hydrothermal synthesis. *Acc. Chem. Res.* **2001**, *34*, 239–247.

(4) Kanatzidis, M. G.; Pöttgen, R.; Jeitschko, W. The metal flux: a preparative tool for the exploration of intermetallic compounds. *Angew. Chem. Int.* **2005**, *44*, 6996–7023.

(5) Bonneau, P. R.; Jarvis, R. F.; Kaner, R. B. Rapid solid-state synthesis of materials from molybdenum disulphide to refractories. *Nature* **1991**, *349*, 510–512.

(6) Mandal, T. K.; Gopalakrishnan, J. From rocksalt to perovskite: a metathesis route for the synthesis of perovskite oxides of current interest. *J. Mater. Chem.* **2004**, *14*, 1273.

(7) Nénert, G.; Pollet, M.; Marinel, S.; Blake, G.; Meetsma, A.; Palstra, T. T. Experimental evidence for an intermediate phase in the multiferroic $YMnO_3$. *J. Phys. Condensed Matter* **2007**, *19*, 466212.

(8) Chen, Y.; Ma, Y.; Wang, Z.; Wang, X.; Liu, H.; Cheng, G. J. Molten salt synthesis of $YMnO_3$ powder with high near-infrared reflectivity. *Mater. Lett.* **2018**, *229*, 171–173.

(9) Todd, P. K.; Smith, A. M.; Neilson, J. R. Yttrium Manganese Oxide Phase Stability and Selectivity Using Lithium Carbonate Assisted Metathesis Reactions. *Inorg. Chem.* **2019**, *58*, 15166–15174.

(10) Todd, P. K.; Neilson, J. R. Selective formation of yttrium manganese oxides through kinetically competent assisted metathesis reactions. *J. Am. Chem. Soc.* **2019**, *141*, 1191–1195.

(11) Todd, P. K.; Wustrow, A.; McAuliffe, R. D.; McDermott, M. J.; Tran, G. T.; McBride, B. C.; Boeding, E. D.; O'Nolan, D.; Liu, C.-H.; Dwaraknath, S. S., et al. Defect-Accommodating Intermediates Yield Selective Low-Temperature Synthesis of YMnO3 Polymorphs. *Inorg. Chem.* **2020**, *59*, 13639–13650.

(12) Van Aken, B. B.; Meetsma, A.; Palstra, T. T. Hexagonal $YMnO_3$. *Acta Cryst. C* **2001**, *57*, 230–232.

(13) Uusi-Esko, K.; Malm, J.; Imamura, N.; Yamauchi, H.; Karppinen, M. Characterization of $RMnO_3$ (R= Sc, Y, Dy-Lu): High-pressure synthesized metastable perovskites and their hexagonal precursor phases. *Mater. Chem. Phys.* **2008**, *112*, 1029–1034.

(14) Kamata, K.; Nakajima, T.; Nakamura, T. Thermogravimetric study of rare earth manganites $AMnO_3$ (A= Sm, Dy, Y, Er, Yb) at 1200° C. *Mater. Res. Bull.* **1979**, *14*, 1007–1012.

(15) Giaquinta, D. M.; zur Loye, H.-C. Structural Predictions in the ABO_3 Phase Diagram. *Chem. Mater.* **1994**, *6*, 365–372.

(16) Brinks, H.; Fjellvåg, H.; Kjekshus, A. Synthesis of Metastable Perovskite-type $YMnO_3$ and $HoMnO_3$. *J. Sol. State Chem.* **1997**, *129*, 334 – 340.

(17) O'Nolan, D.; Huang, G.; Kamm, G. E.; Grenier, A.; Liu, C.-H.; Todd, P. K.; Wustrow, A.; Thinh Tran, G.; Montiel, D.; Neilson, J. R., et al. A thermal-gradient approach to variable-temperature measurements resolved in space. *J. Appl. Cryst.* **2020**, *53*, 662–670.

(18) Wendlandt, W. W. The thermal decomposition of yttrium, scandium, and some rare-earth chloride hydrates. *J. Inorg. Nuc. Chem.* **1957**, *5*, 118–122.

(19) Ling, C. D.; Neumeier, J.; Argyriou, D. N. Observation of antiferromagnetism in marokite $CaMn_2O_4$. *J. Solid State Chem.* **2001**, *160*, 167–173.

(20) Truong, Q. D.; Kobayashi, H.; Nayuki, K.; Sasaki, Y.; Honma, I. Atomic-scale observation of phase transition of $MgMn_2O_4$ cubic spinel upon the charging in Mg-ion battery. *Solid State Ionics* **2020**, *344*, 115136.

(21) Wang, J.; Toby, B. H.; Lee, P. L.; Ribaud, L.; Antao, S. M.; Kurtz, C.; Ramanathan, M.; Von Dreele, R. B.; Beno, M. A. A dedicated powder diffraction beamline at the advanced photon source: commissioning and early operational results. *Rev. Sci. Inst.* **2008**, *79*, 085105.

(22) Pathak, P.; Vasavada, N. Thermal expansion of NaCl, KCl and CsBr by X-ray diffraction and the law of corresponding states. *Acta Cryst. A* **1970**, *26*, 655–658.

(23) Wright, C. J. Towards Real Time Characterization of Grain Growth from the Melt. Ph.D. thesis, Columbia University, 2020, 52–60.

(24) Kresse, G.; FurthmÃ¼ller, J. Efficiency of ab-initio total energy calculations for metals and semiconductors using a plane-wave basis set. *Comput. Mater. Sci.* **1996**, *6*, 15–50.

(25) Perdew, J. P.; Burke, K.; Ernzerhof, M. Generalized Gradient Approximation Made Simple. *Phys. Rev. Lett.* **1996**, *77*, 3865–3868.

(26) Wang, L.; Maxisch, T.; Ceder, G. Oxidation energies of transition metal oxides within the GGA+U framework. *Phys. Rev. B* **2006**, *73*, 195107.

(27) Blöchl, P. E. Projector augmented-wave method. *Phys. Rev. B* **1994**, *50*, 17953–17979.

(28) Kresse, G.; Joubert, D. From ultrasoft pseudopotentials to the projector augmented-wave method. *Phys. Rev. B* **1999**, *59*, 1758.

(29) Jain, A.; Ong, S. P.; Hautier, G.; Chen, W.; Richards, W. D.; Dacek, S.; Cholia, S.; Gunter, D.; Skinner, D.; Ceder, G.; Persson, K. A. Commentary: The Materials Project: A materials genome approach to accelerating materials innovation. *APL Mater.* **2013**, *1*, 011002.

(30) Horton, M. K.; Montoya, J. H.; Liu, M.; Persson, K. A. High-throughput prediction of the ground-state collinear magnetic order of inorganic materials using Density Functional Theory. *NPJ Computational Mater.* **2019**, *5*, 1–11.

(31) Freysoldt, C.; Neugebauer, J.; Van de Walle, C. G. Fully Ab Initio Finite-Size Corrections for Charged-Defect Supercell Calculations. *Phys. Rev. Lett.* **2009**, *102*, 016402.

(32) Freysoldt, C.; Grabowski, B.; Hickel, T.; Neugebauer, J.; Kresse, G.; Janotti, A.; Van de Walle, C. G. First-principles calculations for point defects in solids. *Rev. Mod. Phys.* **2014**, *86*, 253–305.

(33) Broberg, D.; Medasani, B.; Zimmermann, N. E.; Yu, G.; Canning, A.; Haranczyk, M.; Asta, M.; Hautier, G. PyCDT: A Python toolkit for modeling point defects in semiconductors and insulators. *Computer Phys. Comm.* **2018**, *226*, 165–179.

(34) Mathew, K. et al. Atomate: A high-level interface to generate, execute, and analyze computational materials science workflows. *Comput. Mater. Sci.* **2017**, *139*, 140 – 152.

(35) Ong, S. P.; Richards, W. D.; Jain, A.; Hautier, G.; Kocher, M.; Cholia, S.; Gunter, D.; Chevrier, V. L.; Persson, K. A.; Ceder, G. Python Materials Genomics (pymatgen): A robust, open-source python library for materials analysis. *Comput. Mater. Sci.* **2013**, *68*, 314–319.

(36) Bartel, C. J.; Millican, S. L.; Deml, A. M.; Rumptz, J. R.; Tumas, W.; Weimer, A. W.; Lany, S.; Stevanović, V.; Musgrave, C. B.; Holder, A. M. Physical descriptor for the Gibbs energy of inorganic crystalline solids and temperature-dependent materials chemistry. *Nat. Commun.* **2018**, *9*, 4168.

(37) Malcolm W. Chase, J. *NIST-JANAF thermochemical tables*; Fourth edition. Washington, DC: American Chemical Society; New York: American Institute of Physics for the National Institute of Standards and Technology, 1998, 695,812.

(38) *Heat Transfer Module User's Guide*; COMSOL Multiphysics® v. 5.4. COMSOL AB, Stockholm, Sweden., 2018.

(39) FTsalt FACT Salt Databases. http://www.factsage.cn/fact/documentation/FTsalt/FTsalt_Figs.htm (Accessed 2021-03-22), $CaCl_2$/$MgCl_2$ Phase Diagram.

(40) Bugaris, D. E.; zur Loye, H.-C. Materials discovery by flux crystal growth: quaternary and higher order oxides. *Angew. Chem. Int.* **2012**, *51*, 3780–3811.

(41) Lindemann, F. A. Ueber die berechnung molekularer eigenfrequenzen. *Phys. Z* **1910**, *11*, 609–612.

(42) Frenken, J. W.; Van der Veen, J. Observation of surface melting. *Phys. Rev. Lett.* **1985**, *54*, 134.

(43) Marks, L.; Chiaramonti, A.; Rahman, S.; Castell, M. Transition from order to configurational disorder for surface reconstructions on $SrTiO_3$ (111). *Phys. Rev. Lett.* **2015**, *114*, 226101.

(44) Zhou, Y.; Vitkup, D.; Karplus, M. Native proteins are surface-molten solids: application of the Lindemann criterion for the solid versus liquid state. *J. Mol. Biol.* **1999**, *285*, 1371–1375.

(45) Bale, C. W.; Chartrand, P.; Degterov, S.; Eriksson, G.; Hack, K.; Mahfoud, R. B.; Melançon, J.; Pelton, A.; Petersen, S. FactSage thermochemical software and databases. *calphad* **2002**, *26*, 189–228.

(46) Moure, C.; Villegas, M.; Fernandez, J.; Tartaj, J.; Duran, P. Phase transition and electrical conductivity in the system $YMnO_3$-$CaMnO_3$. *J. Mater. Sci.* **1999**, *34*, 2565–2568.

(47) Sattibabu, B.; Bhatnagar, A. K.; Mohan, D.; Das, D.; Sundararaman, M.; Siruguri, V.; Rayaprol, S. Low temperature magnetic properties of magnesium substituted $YbMnO_3$. AIP Conference Proceedings. 2014; pp 1766–1768.

(48) Bosak, A.; Kamenev, A.; Graboy, I.; Antonov, S.; Gorbenko, O.; Kaul, A.; Dubourdieu, C.; Senateur, J.; Svechnikov, V.; Zandbergen, H.; Holländer, B. Epitaxial phase stabilisation phenomena in rare earth manganites. *Thin Solid Films* **2001**, *400*, 149 – 153, Proceedings of Symposium N on Ultrathin Oxides.

(49) Alonso, J.; Martinez-Lope, M.; Casais, M.; Fernandez-Diaz, M. Evolution of the Jahn- Teller distortion of MnO_6 octahedra in $RMnO_3$ perovskites (R= Pr, Nd, Dy, Tb, Ho, Er, Y): a neutron diffraction study. *Inorg. Chem.* **2000**, *39*, 917–923.

(50) Wood, V.; Austin, A.; Collings, E.; Brog, K. Magnetic properties of heavy-rare-earth orthomanganites. *J. Phys. Chem. Solids* **1973**, *34*, 859–868.

Graphical TOC Entry